

LHC-friendly freeze-in dark matter via Higgs portal

Xinyue Yin,^{a,*} Shuai Xu,^{b,†} and Sibozheng^{a,‡}

^aDepartment of Physics, Chongqing University, Chongqing 401331, China

^bSchool of Physics and Telecommunications Engineering, Zhoukou Normal University,
Henan 466001, China

Abstract

It is known that single-field freeze-in dark matter barely leaves footprints in dark matter direct detection and collider experiments. This situation can be altered in two-field context. In this work we propose a two-field freeze-in dark matter model through Higgs portal. The observed dark matter relic abundance is obtained by a decay of scalar mediator thermalized in the early Universe. While there is a lack of direct dark matter signals, the scalar mediator is in the reach of HL-LHC either through vector boson fusion or Mono-Z channel. Within allowed scalar mass window of 10-50 GeV, we use improved cuts to derive both 2σ exclusion and 5σ discovery limits, depending on the value of Higgs portal coupling. If verified, this scalar mediator signal allows us to infer the freeze-in dark matter.

*yinxu@stu.cqu.edu.cn

†xushuai@zknmu.edu.cn

‡sibozheng.zju@gmail.com (corresponding author)

Contents

1	Introduction	1
2	Dark matter phenomenology	3
2.1	Relic abundance	3
2.2	Direct detections	5
2.3	Indirect detections	6
3	LHC phenomenology	6
3.1	Indirect detection	6
3.2	Direct detection	6
3.2.1	Productions	7
3.2.2	Cuts	7
3.2.3	Sensitivities of HL-LHC	9
4	Conclusion	11
A	Selection of cuts	12

1 Introduction

Due to current experimental status of thermal dark matter (DM), there is a growing interest in non-thermal DM. Non-thermal DM can be produced in a few different ways such as well understood freeze-in mechanism [1].¹ Single-field examples of freeze-in DM (FIDM) include axion-like scalar [2, 3], sterile neutrino fermion [4–7] and dark photon [8], some of which are well motivated by new physics beyond Standard Model (SM). A common feature of these FIDM models is a lack of signals at DM direct detection and collider experiments, as a result of feeble DM coupling to the SM sector. Within DM mass range larger than MeV scale, only cosmic [9, 10] or astrophysical [11–14] ray data has touched on this type of DM parameter space so far.

The situation changes in two-field FIDM. A two-field FIDM, which contains DM and its force mediator, can be constructed in three different ways, depending on how to assign the feeble interaction. Explicitly,

- The first case is to choose a feeble interaction between the DM and SM sector but a

¹An alternative mechanism is through gravitational portal (during) after inflation, which is beyond the scope of this work.

strong coupling between the DM and force mediator. Ref.[15] has used this case to resolve the small-scale problem related to collisionless cold DM.

- In the second case, one can choose a feeble interaction between the force mediator and SM sector but a strong coupling between the DM and force mediator. A representative example is dark photon mediated DM, which has been used to explain EDGES 21-cm anomaly [16, 17] and small-scale problem [18] respectively.
- In the third case, one can adopt a feeble interaction between the DM and force mediator but a strong coupling between the force mediator and SM sector. In this situation, collider-friendly FIDM models [19–22] can be constructed.

In this work, we investigate a new two-field FIDM of the third type with the following Lagrangian

$$\mathcal{L}_D = i\bar{\psi}(\gamma^\nu\partial_\nu - m_\psi)\psi + \frac{1}{2}\partial_\mu s\partial^\mu s - \frac{\mu_s^2}{2}s^2 - \lambda\bar{\psi}\psi s - \kappa s^2 |H|^2, \quad (1)$$

where fermion ψ and real singlet scalar s is the DM and force mediator respectively, and H is the SM Higgs doublet. We impose a Z_2 dark parity on the dark sector, under which

$$Z_2 : s \rightarrow -s, \quad \psi \rightarrow -\psi, \quad (2)$$

and the SM sector is even.² We further assume this parity to be broken by the renormalizable Yukawa interaction in the dark sector, which suggests the magnitude of λ being small by following the argument of naturalness [23]. Unlike in the Higgs-portal scalar DM [24–26] based on freeze-out mechanism, where only a narrow scalar mass window near a half of the Higgs mass is not excluded [27, 28], the FIDM due to a small λ in eq.(1) allows us to reopen the scalar mass window above GeV scale. Within this mass window, the scalar mediator which only decays to a pair of DM particles contributes to observable missing energy [29] at the LHC for κ being not far away from unity, making our model differ from previous two-field models [19–22] where the mediator therein decays to either SM lepton or hadron final states.

The rest of this paper is organized as follows. In Sec.2 we discuss DM phenomenology including DM production, scattering off SM protons, and annihilation into SM particles. Although there is a lack of DM signals in traditional DM detection experiments, the scalar mediator can leave footprints in the LHC, depending on the value of Higgs portal coupling κ . Sec.3 is devoted to investigate high luminosity (HL)-LHC reaches of the scalar mediator in allowed scalar mediator mass range of 10 – 60 GeV through the Higgs portal induced vector boson fusion (VBF) and Mono-Z channel, where both 2σ exclusion and 5σ discovery limits are presented. Appendix.A shows details of how to improve cuts than those of [29]. Finally, we conclude in Sec.4.

²We neglect the s^4 term which does not affect either DM or collider phenomenological analysis throughout this paper.

2 Dark matter phenomenology

In this section we begin with the DM phenomenology in DM parameter space composed of $\{m_\psi, m_s, \lambda\}$ in eq.(1) with a negligible dependence on κ for κ larger than $\sim 10^{-6}$ required by the freeze-out mechanism, where the scalar mass squared $m_s^2 = \mu_s^2 + \kappa v^2 \geq \kappa v^2$ with the electroweak scale $v = 246$ GeV.

2.1 Relic abundance

With κ being large enough, the scalar mediator keeps thermal equilibrium with SM thermal bath. In contrast, for a tiny λ the DM is produced in the early Universe through the freeze-in mechanism with Boltzmann equation

$$\dot{n}_\psi + 3Hn_\psi = \mathcal{C}, \quad (3)$$

where n_ψ is the DM number density, H is the Hubble rate due to cosmic expansion, and \mathcal{C} is the ‘‘collision’’ term mainly arising from (a) decay $s \rightarrow \psi\bar{\psi}$ in the DM mass range of $m_s > 2m_\psi$ considered here and (b) two-body annihilation $h s \rightarrow \psi\bar{\psi}$ via the κ coupling.

To see which process dominates the \mathcal{C} term in eq.(3), we present in fig.1 the individual contribution to DM yield $Y_\psi \equiv n_\psi/S$ as function of m_ψ with S the entropy of SM thermal bath, for a set of fixed values $\kappa = 1$, $\lambda = \{10^{-12}, 10^{-11}\}$ and $2m_\psi < m_s = 10$ GeV. In this plot (a) and (b) is shown in solid and dashed, respectively.

- The decay induced contribution to Y_ψ is consistent with an analytic approximation [1]

$$Y_\psi \approx \frac{135}{4\pi^3 \cdot 1.66g_{s,*}\sqrt{g_{\rho,*}}} \frac{M_P \Gamma_s}{m_s^2}, \quad (4)$$

where $g_{s,*}$ and $g_{\rho,*}$ are the number of degrees of freedom in entropy and energy density respectively, M_P is the non-reduced Planck mass, and the scalar mediator decay width

$$\Gamma_s(s \rightarrow \psi\bar{\psi}) = \frac{\lambda^2}{8\pi} m_s \left(1 - \frac{4m_\psi^2}{m_s^2}\right)^{3/2}. \quad (5)$$

- The annihilation induced contribution to Y_ψ is proportional to $\sim \lambda^2 \kappa^2$. As seen in fig.1, this contribution is smaller than the decay induced one by more than two orders, which is further reduced by choosing κ smaller than unity.

Therefore, in the parameter regions with $10^{-6} < \kappa \leq 1$ and $2m_\psi < m_s < 1$ TeV considered in this paper the DM freeze-in production in the early Universe is dominated by the scalar decay process.

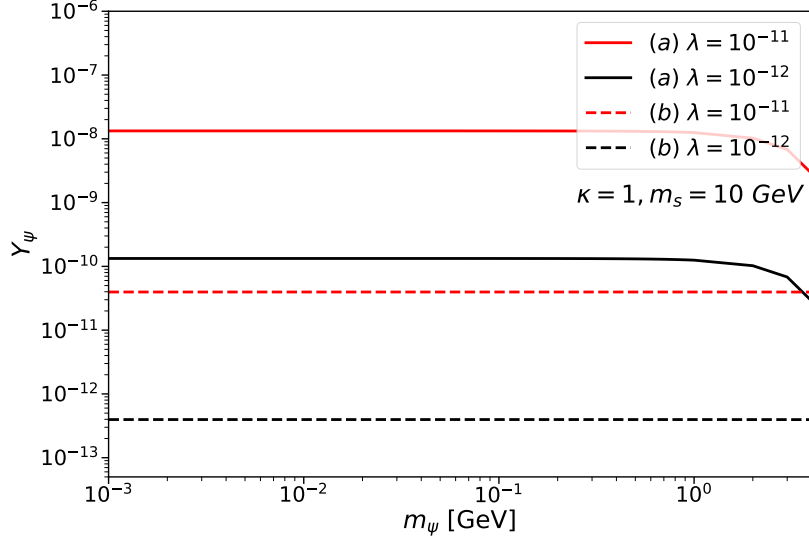


Figure 1: An illustration of the individual contribution to Y_ψ as function of m_ψ for a set of fixed values $\kappa = 1$, $\lambda = \{10^{-12}, 10^{-11}\}$ and $2m_\psi < m_s = 10$ GeV, where (a) and (b) is shown in solid and dashed, respectively.

In terms of publicly available code `micrOMEGAs6.0` [31], we show in fig.2 contours of the observed relic density $\Omega_\psi h^2 = 0.12 \pm 0.001$ [30] projected to the plane of $m_s - m_\psi$ for various values of $10^{11}\lambda = \{1, 3, 5\}$, where the shaded region is excluded by $2m_\psi < m_s$. The numerical results of fig.2 are consistent with the analytic approximation

$$\Omega_\psi h^2 = \frac{m_\psi Y_\psi S_0}{\rho_{\text{crit},0}} \approx 0.1 \left(\frac{\lambda}{5 \times 10^{-13}} \right)^2 \left(\frac{m_\psi}{m_s} \right), \quad (6)$$

derived from eq.(4), where S_0 is the present value of S and $\rho_{\text{crit},0}$ is the critical energy density. Take an explicit value of $\lambda = 5 \times 10^{-11}$ for example, in which case $m_s/m_\psi \sim 10^4$ as shown by the red curve is verified by eq.(6). On the other hand, eq.(6) suggests that a curve with respect to a larger λ should have a larger slope, which is also justified by comparing the curves in this plot.

The contours of $\Omega_\psi h^2$ in fig.2 barely depend on κ ; see also eq.(6). This is true as long as κ is larger than the threshold value $\sim 10^{-6}$ required to keep the scalar mediator in thermal equilibrium with the SM thermal bath. In this situation, κ only affects the DM relic density through altering the values of $g_{s,*}$ and $g_{\rho,*}$ in eq.(4) by $\sim 1\%$, which can be safely neglected.

Before closing the analysis on the DM relic density, we remind that the scalar mediator lifetime is

$$\tau_s \sim 10 \text{ sec} \left(\frac{\lambda}{10^{-12}} \right)^{-2} \left(\frac{m_s}{1 \text{ GeV}} \right)^{-1}, \quad (7)$$

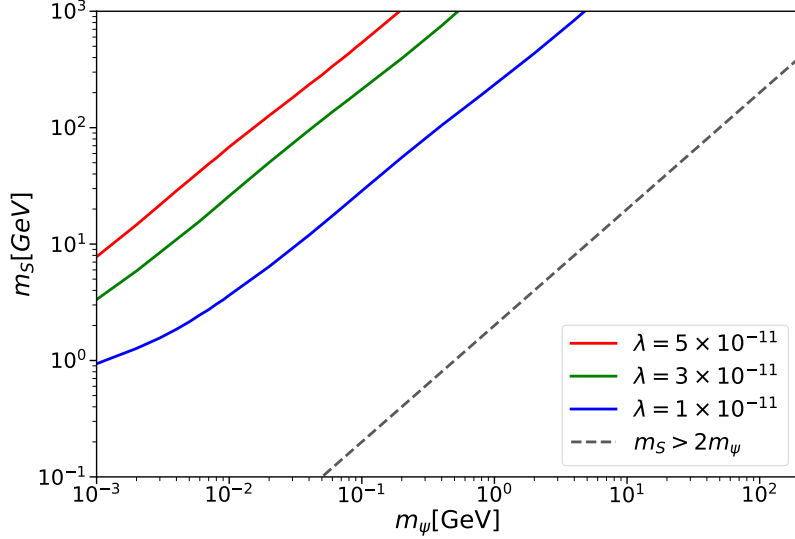


Figure 2: Contours of the observed DM relic abundance projected to the plane of $m_s - m_\psi$ for various values of λ , where the shaded region is excluded by $2m_\psi < m_s$ and the top left region with $\lambda \sim 10^{-11}$ and $m_s \geq 1$ GeV evades the BBN constraint on τ_s .

using eq.(5). Eq.(7) shows that the lifetime is always shorter than $\sim 10^4$ sec, when the big-bang nucleosynthesis (BBN) takes place, in the top left region of fig.2 with $\lambda \sim 10^{-11}$ and $m_s \geq 1$ GeV, which evades the BBN constraint [32, 33].

2.2 Direct detections

In our model the DM scatters off protons or electrons by one-loop Feynman diagram. Consider that the electron Yukawa coupling is small, we focus on spin-independent DM-proton cross section σ_{SI} . It can be estimated by a non-relativistic effective operator analysis in low energy region. Integrating out the scalar mediator in eq.(1), one finds

$$\mathcal{L}_{\text{eff}} \sim \kappa \lambda^2 \frac{m_\psi^3}{m_s^4} \psi \bar{\psi} |H|^2 + \dots, \quad (8)$$

which gives

$$\sigma_{\text{SI}} \sim 10^{-86} \text{cm}^2 \cdot \kappa^2 \cdot \left(\frac{\lambda}{10^{-11}} \right)^4, \quad (9)$$

for the reference masses $m_s \sim m_\psi \sim 100$ GeV. Normalized to $\kappa = 1$, the value of σ_{SI} suppressed by λ^4 is roughly ~ 42 orders of magnitude smaller than the latest XENON1T [34], PandaX-4T [35] and LZ [36] bounds. Note, while the effective operator analysis in eq.(8) is not concrete, the rough estimate on the magnitude of σ_{SI} via eq.(9) holds.

2.3 Indirect detections

As mentioned in the Introduction, so far the measurements of astrophysical or cosmic rays place the most stringent constraints on DM annihilation cross sections within the DM mass range of $m_\psi > 1$ MeV. Take the $e\bar{e}$ final states for example, with respect to which the DM annihilation cross section reads as

$$\sigma_{\text{ann}}(\psi\bar{\psi} \rightarrow e\bar{e})v_{\text{rel}} \sim 10^{-68} \text{cm}^3 \text{s}^{-1} \cdot \kappa^2 \cdot \left(\frac{\lambda}{10^{-11}} \right)^4, \quad (10)$$

for the reference mass $m_\psi \sim 100$ GeV by using eq.(8), where v_{rel} is the relative velocity of two incoming DM particles. Due to the λ^4 suppression, the value of $\sigma_{\text{ann}}(\psi\bar{\psi} \rightarrow e\bar{e})v_{\text{rel}}$ in eq.(10) is roughly ~ 38 orders of magnitude smaller than current cosmic ray bounds, see e.g [9].

3 LHC phenomenology

While it is unlikely to probe the freeze-in DM at the DM detection facilities, the scalar mediator s which only decays to a pair of DM particles can be probed by the LHC, given the κ coupling to Higgs being large enough. In this section, we firstly discuss current LHC limit on Higgs invisible decay, then turn to HL-LHC reaches of s with center-of-mass energy fixed to be 14 TeV.

3.1 Indirect detection

For $2m_s < m_h$ with m_h the observed Higgs mass, the scalar mediator contributes to the invisible decay of Higgs with decay width

$$\Gamma_h^{\text{inv}}(h \rightarrow ss) = \frac{\kappa^2 v^2}{8\pi m_h} \sqrt{1 - \frac{4m_s^2}{m_h^2}}, \quad (11)$$

which is upper bounded as $\Gamma_h^{\text{inv}} \leq 0.26 \Gamma_h$ at 95% CL [37] with the Higgs decay width $\Gamma_h \approx 4.15$ MeV.

3.2 Direct detection

Given the κ coupling between s and H , the scalar mediator can be produced through both VBF and Mono-Z channel similar to the Higgs-portal scalar DM [29]. As mentioned in the Introduction, unlike in [29] where only $m_s \sim m_h/2$ is not excluded, our model reopens a larger mass window of $m_s \geq 1$ GeV.

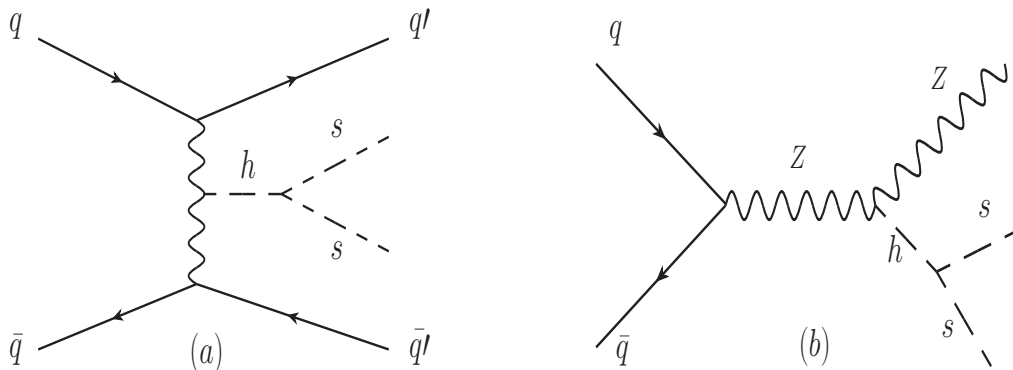


Figure 3: The leading-order Feynman diagram with respect to (a) VBF and (b) Mono-Z channel at the LHC, respectively.

3.2.1 Productions

VBF. The VBF channel corresponds to $q\bar{q} \rightarrow h^* + jj \rightarrow ss + jj$ as shown in the plot (a) of fig.3, where q and q' refers to quarks, and s contributes to a large missing energy (MET). We present in the left plot of fig.4 the values of signal cross section $\sigma_{s,\text{VBF}}$ as function of m_s for various values of $\kappa = \{10^{-3}, 10^{-2}, 10^{-1}, 1\}$ at the 14-TeV LHC. In this plot, the magnitudes of $\sigma_{s,\text{VBF}}$ vary over six orders from $m_s = 10$ GeV to 100 GeV for a fixed value of κ , which significantly decrease at $m_s \sim m_h/2$. With respect to this VBF channel, the SM background is given by $q\bar{q} \rightarrow W/Z + \text{jets}$, with an explicit value of cross section $\sigma_{b,\text{VBF}} \approx 6.4 (1.2) \times 10^4$ pb for the $W(Z) + 2$ jets final states, implying that a large portion of the parameter regions with $m_s \sim 10 - 100$ GeV and $\kappa \sim 10^{-3} - 1$ is in the reach of HL-LHC.

Mono - Z. The Mono-Z channel refers to $q\bar{q} \rightarrow h^* + Z \rightarrow ss + Z$ as shown in the plot (b) of fig.3, where the Z boson can decay into a pair of leptons. The right plot of fig.4 shows the values of signal cross section $\sigma_{s,\text{MZ}}$ as function of m_s for various values of $\kappa = \{10^{-3}, 10^{-2}, 10^{-1}, 1\}$ at the 14-TeV LHC. In this plot, the magnitudes of $\sigma_{s,\text{MZ}}$ have a dramatical decline at $m_s \sim m_h/2$ similar to the left plot of fig.4, despite being smaller. Regarding this Mono-Z channel, the SM background is given by $q\bar{q} \rightarrow ZZ$ with cross section $\sigma_{b,\text{MZ}} \approx 30$ pb, where one Z boson decays into $\nu\bar{\nu}$ and the other Z to $\ell\bar{\ell}$ with $\ell = e, \mu$ respectively. Compared with the VBF channel, the mono-Z channel is sub-leading but relatively cleaner. Likewise, a large portion of the parameter regions with $m_s \sim 10 - 100$ GeV and $\kappa \sim 10^{-3} - 1$ can be also reached by the HL-LHC.

3.2.2 Cuts

VBF. Ref.[29] has applied the earlier CMS cuts in [38] to a numerical stimulation of the scalar DM via the VBF channel. Those cuts give a ratio of $\epsilon_s/\sqrt{\epsilon_b} \sim 5$ for a million events, where ϵ_s and ϵ_b refers to signal and background efficiency respectively. In this work we make

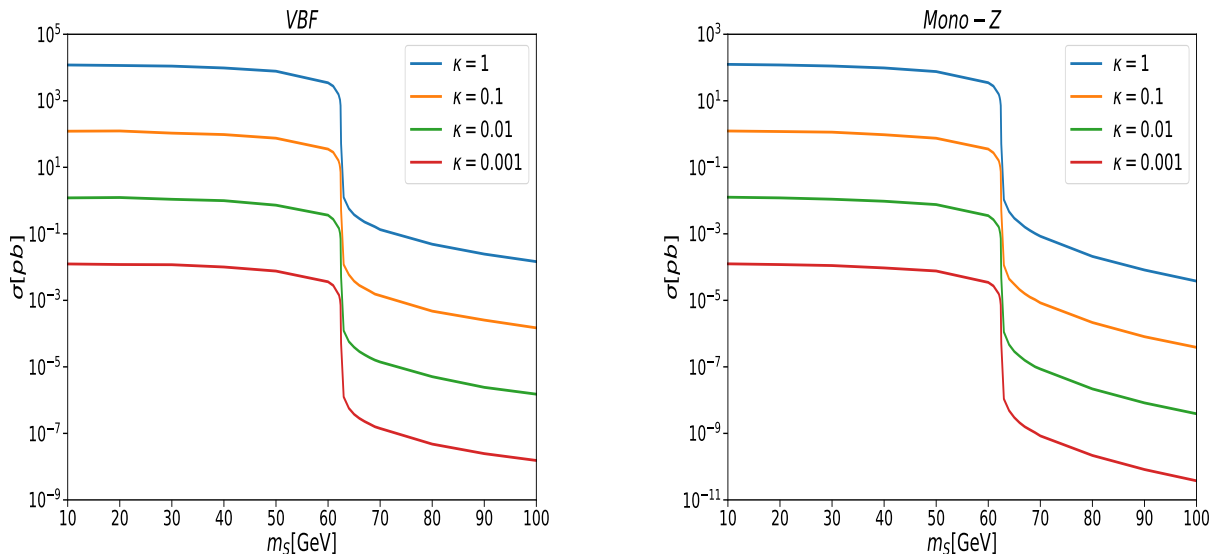


Figure 4: Values of signal cross section $\sigma_{s,\text{VBF}}$ (left) and $\sigma_{s,\text{MZ}}$ (right) as function of m_s for various values of $\kappa = \{10^{-3}, 10^{-2}, 10^{-1}, 1\}$ at the 14-TeV LHC, which have a significant decline at $m_s \sim m_h/2$.

use of recently reported CMS [39] and ATLAS [40] cuts to update the stimulation of VBF channel. Explicitly,

- We use `MadAnalysis` [41] to analyze the distribution of both signal and background events as function of relevant parameters, which is explicitly shown in fig.7 of appendix.A.
- Then we refer the cuts used in [39, 40] to choose the explicit values of these cut parameters one by one. During this process, when a new added cut such as azimuthal angle $\Delta\phi$ between the two jets does not offer an effective increase in the ratio of $\epsilon_s/\sqrt{\epsilon_b}$ but obviously reduces the number of signal events, we will neglect that cut parameter.

Table.1 shows the final cuts applied to the VBF channel, where $N(\text{jet})$ is the number of jets, $N(\ell)$ the number of leptons, $P_T^{j_{1(2)}}$ and $\eta_{j_{1(2)}}$ the transverse momentum and pseudorapidity of the first (second) leading jet respectively, M_{jj} invariant mass of the two leading jets, E_T^{miss} the missing transverse energy, and $\Delta R_{jj} = \sqrt{(\Delta\phi)^2 + (\Delta\eta)^2}$ with $\Delta\eta$ the pseudorapidity difference between the two leading jets. In terms of the set of cuts in Table.1, the value of $\epsilon_s/\sqrt{\epsilon_b}$ is enhanced by $\sim 3 - 4$ times compared to that of ref.[29].

Mono - Z. Using the earlier CMS cuts in [42] that give a ratio of $\epsilon_s/\sqrt{\epsilon_b} \sim 15$ for a million events, ref.[29] also analyzed the scalar DM reach via the Mono-Z channel at the HL-LHC. Now we repeat this analysis for the scalar mediator by referring to updated cuts in [43–45]. To do so,

VBF	Mono-Z
$N(\text{jet}) \geq 2$	$N(\ell)=2, \ell = e, \mu$
$N(\ell) = 0$	$P_T^{\ell\ell} > 150 \text{ GeV}$
$P_T^{j_1} > 60 \text{ GeV}$	$ M_{\ell\ell} - m_Z > 10 \text{ GeV}$
$ \eta_{j_2} > 3$	$E_T^{\text{miss}} > 180 \text{ GeV}$
$E_T^{\text{miss}} > 100 \text{ GeV}$	$ E_T^{\text{miss}} - P_T^{\ell\ell} / P_T^{\ell\ell} < 1$
$M_{jj} > 1100 \text{ GeV}$	$\Delta\phi(\vec{P}_T^{\ell\ell}, \vec{P}_T^{\text{miss}}) > 2.5 \text{ rad}$
$\Delta R_{jj} > 5.5$	$\Delta R_{\ell\ell} < 1$

Table 1: Cuts adopted for numerical stimulations of the VBF (left) and Mono-Z (right) channel, respectively.

- Firstly, we only pick cut parameters specified for the lepton pair $\ell\bar{\ell}$ with $\ell = e, \mu$ and neglect those related to $\ell = \tau$ and jets.
- Secondly, we use `MadAnalysis` [41] to carry out the distribution of both signal and background events as function of the selected cuts, which is shown in fig.8 of appendix.A. Repeating the same process as in the VBF channel, we choose the explicit values of these cut parameters one by one.

Table.1 shows the final cuts applied to the Mono-Z channel, where $N(\ell) = 2$ is the number of leptons, $P_T^{\ell\ell}$ the dilepton transverse momentum, $M_{\ell\ell}$ the dilepton mass, $\Delta\phi(\vec{P}_T^{\ell\ell}, \vec{P}_T^{\text{miss}})$ the azimuthal separation between dilepton and missing momentum, and $\Delta R_{\ell\ell}$ the separation between two leptons. The set of cuts in Table.1 yield an enhancement on the ratio of $\epsilon_s/\sqrt{\epsilon_b}$ by $\sim 2 - 3$ times compared to ref.[29].

3.2.3 Sensitivities of HL-LHC

Collecting the previous results about the cross sections and efficiencies, we now present the 2σ exclusion (5σ discovery) defined as

$$\frac{S}{\sqrt{B}} \left(\frac{S}{\sqrt{S+B}} \right) = 2 \quad (5), \quad (12)$$

where S and B is the number of signal and background events, respectively.

VBF. Fig.5 shows the 2σ exclusion (in solid) and 5σ discovery (in dashed) of HL-LHC projected to the plane of (m_s, κ) for two different values of integrated luminosity $\mathcal{L} = \{3, 10\}$ ab^{-1} , where significant changes occur at $m_s \sim m_h/2$ as seen in fig.4. In this plot, the black and gray shaded region are excluded by the bound on Γ_h^{inv} in eq.(11) and the scalar mediator mass bound $m_s^2 \geq \kappa v^2$ respectively, pointing to an allowed parameter region with $1 \text{ GeV} < m_s < m_h/2$ and $\kappa \leq 7.5 \times 10^{-3}$. In this region, the range of $\kappa \geq 2.4 (1.5) \times 10^{-3}$

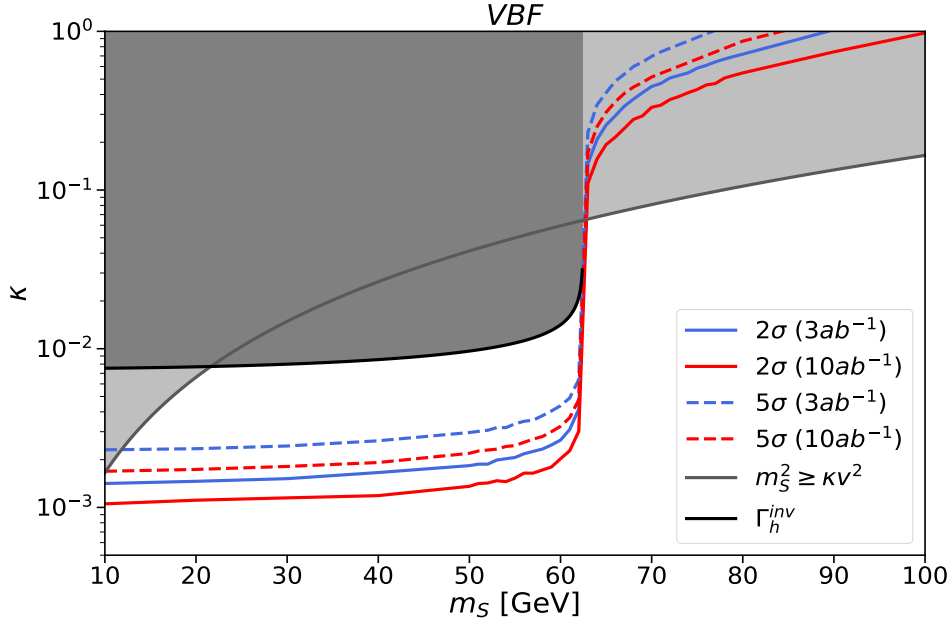


Figure 5: Sensitivities of the HL-LHC with 2σ exclusion (in solid) and 5σ discovery (in dashed) with two different values of integrated luminosity $\mathcal{L} = \{3, 10\} \text{ ab}^{-1}$ for the VBF channel, which are projected to the plane of $m_s - \kappa$ evading the BBN constraint on τ_s in eq.(7). The shaded regions are excluded by the LHC bound on Γ_h^{inv} in eq.(11) (in black) and the scalar mass bound (in gray).

with respect to $m_s \sim 10 - 60 \text{ GeV}$ can be discovered (excluded) for $\mathcal{L} = 3 \text{ ab}^{-1}$, which is slightly improved to $\kappa \geq 1.75 (1.0) \times 10^{-3}$ with a larger value of $\mathcal{L} = 10 \text{ ab}^{-1}$.

Mono – Z. Fig.6 presents the 2σ exclusion (in solid) and 5σ discovery (in dashed) of HL-LHC projected to the plane of (m_s, κ) for $\mathcal{L} = \{3, 10\} \text{ ab}^{-1}$, where both the significant changes in these curves and the shaded regions are the same as in fig.5. Compared to fig.5, given the same \mathcal{L} one sees similar sensitivities of the HL-LHC to the parameter regions in this plot. Explicitly, the range of $\kappa \geq 2.0 (1.25) \times 10^{-3}$ with respect to $m_s \sim 10 - 60 \text{ GeV}$ can be discovered (excluded) for $\mathcal{L} = 3 \text{ ab}^{-1}$, which is improved to $\kappa \geq 1.5 (0.9) \times 10^{-3}$ by the larger $\mathcal{L} = 10 \text{ ab}^{-1}$.

Once detected by the HL-LHC either through the VBF or Mono-Z channel, the scalar signal within the mass window³ of $m_s \sim 10 - 50 \text{ GeV}$ favors an existence of the non-thermal DM as studied in Sec.2, whose mass can be inferred in terms of fig.2 with respect to an explicit value of κ .

³This is beyond the narrow mass window of thermal scalar DM.

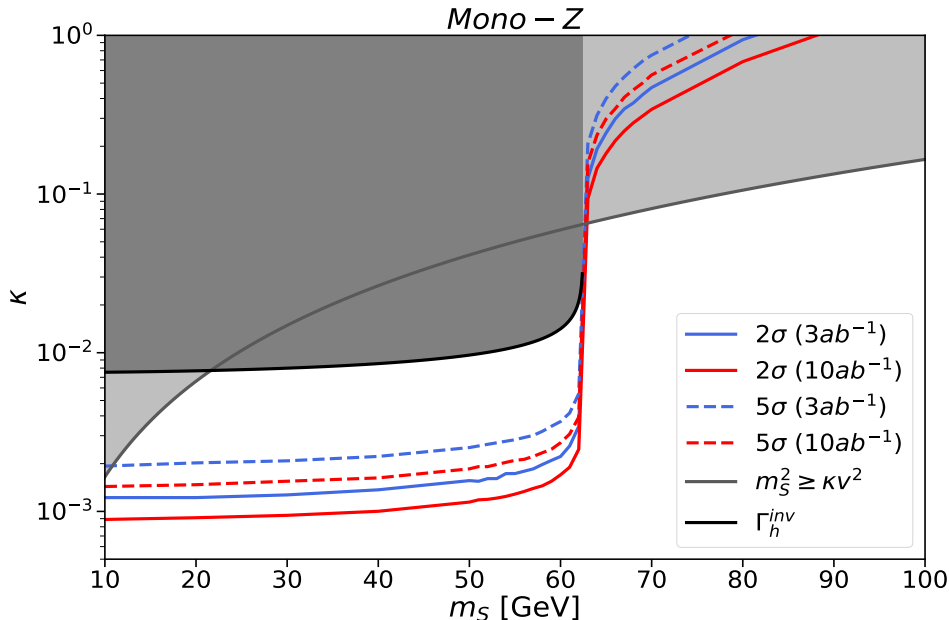


Figure 6: Same as in fig.5 but for the Mono-Z channel.

4 Conclusion

In this work we have revisited the Higgs-portal DM scenario with the DM being non-thermal instead of thermal as previously considered in the literature. Specifically, we have realized this idea in the two-field context, where one is the DM and the other is the scalar mediator coupled to Higgs, with the feeble interaction between them as a result of the Z_2 -parity breaking.

We have divided the model phenomenology analysis into two parts. From the perspective of DM phenomenology, the DM obtains the observed relic density mainly through the decay of scalar mediator thermalized with the SM thermal bath, and has negligible spin-independent scattering and annihilation cross sections as expected in a typical FIDM model. From the perspective of LHC phenomenology, for the Higgs portal coupling being not too far away from unity the scalar mediator can be detected by the LHC. Consider that m_s larger than \sim GeV scale is favored by the BBN constraint, we have reported the HL-LHC reaches of the scalar mediator within the allowed mass window of $m_s \sim 10 - 50$ GeV through both the VBF and Mono-Z channel. If verified, this scalar signal allows us to infer the existence of a non-thermal DM such as ψ proposed here, as interpreting it as the thermal DM has been excluded.

Our study, together with the previous works [19–22], serves as an illustration of rich collider phenomenology in two-field FIDM, compared to the single-field situation. Instead of the Higgs portal considered here, one can use neutrino or vector portal to construct

alternative two-field FIDM models, following our classifications in the Introduction. Different portal may provide unique signals. We left this point for future work.

A Selection of cuts

Fig.7 shows the distribution of VBF signal and background events as function of $p_T^{j_{1(2)}}$, $|\eta_{j_{1(2)}}|$, E_T^{miss} , M_{jj} , $\Delta\phi_{jj}$ and ΔR_{jj} respectively, which illustrates the cut values chosen for the VBF channel in Table.1. For example, imposing $\Delta\phi_{jj}$ or $P_T^{j_2}$ indeed increases the value of $\epsilon_s/\sqrt{\epsilon_b}$ more or less but also leads to a serious suppression on the number of signal events simultaneously. On the contrary, other cuts such $P_T^{j_1} > 60$ GeV can do so with the suppression being affordable.

Likewise, fig.8 shows the distribution of Mono-Z signal and background events as function of P_T^ℓ , $P_T^{\ell\ell}$, $M_{\ell\ell}$, E_T^{miss} , $\Delta\phi(\vec{P}_T^{\ell\ell}, \vec{P}_T^{\text{miss}})$ and $\Delta R_{\ell\ell}$ respectively, which explains the cut values chosen for the Mono-Z channel in Table.1. For example, imposing P_T^ℓ is unable to increase the value of $\epsilon_s/\sqrt{\epsilon_b}$ in an efficient way as explained above, but other cuts such as $P_T^\ell > 150$ GeV can do so.

References

- [1] L. J. Hall, K. Jedamzik, J. March-Russell and S. M. West, JHEP **03** (2010), 080, [arXiv:0911.1120 [hep-ph]].
- [2] K. Langhoff, N. J. Outmezguine and N. L. Rodd, Phys. Rev. Lett. **129**, no.24, 241101 (2022), [arXiv:2209.06216 [hep-ph]].
- [3] M. Jain, A. Maggi, W. Y. Ai and D. J. E. Marsh, [arXiv:2406.01678 [hep-ph]].
- [4] T. Asaka, K. Ishiwata and T. Moroi, Phys. Rev. D **73**, 051301 (2006), [arXiv:hep-ph/0512118 [hep-ph]].
- [5] M. Becker, Eur. Phys. J. C **79**, no.7, 611 (2019), [arXiv:1806.08579 [hep-ph]].
- [6] M. Chianese and S. F. King, JCAP **09**, 027 (2018), [arXiv:1806.10606 [hep-ph]].
- [7] A. Datta, R. Roshan and A. Sil, Phys. Rev. Lett. **127**, no.23, 231801 (2021), [arXiv:2104.02030 [hep-ph]].
- [8] B. Holdom, Phys. Lett. B **166**, 196-198 (1986).
- [9] Z. Xu, Q. Zhou and S. Zheng, Phys. Rev. D **110**, no.11, 115003 (2024), [arXiv:2407.08225 [hep-ph]].
- [10] Z. Xu and S. Zheng, [arXiv:2410.15675 [hep-ph]].

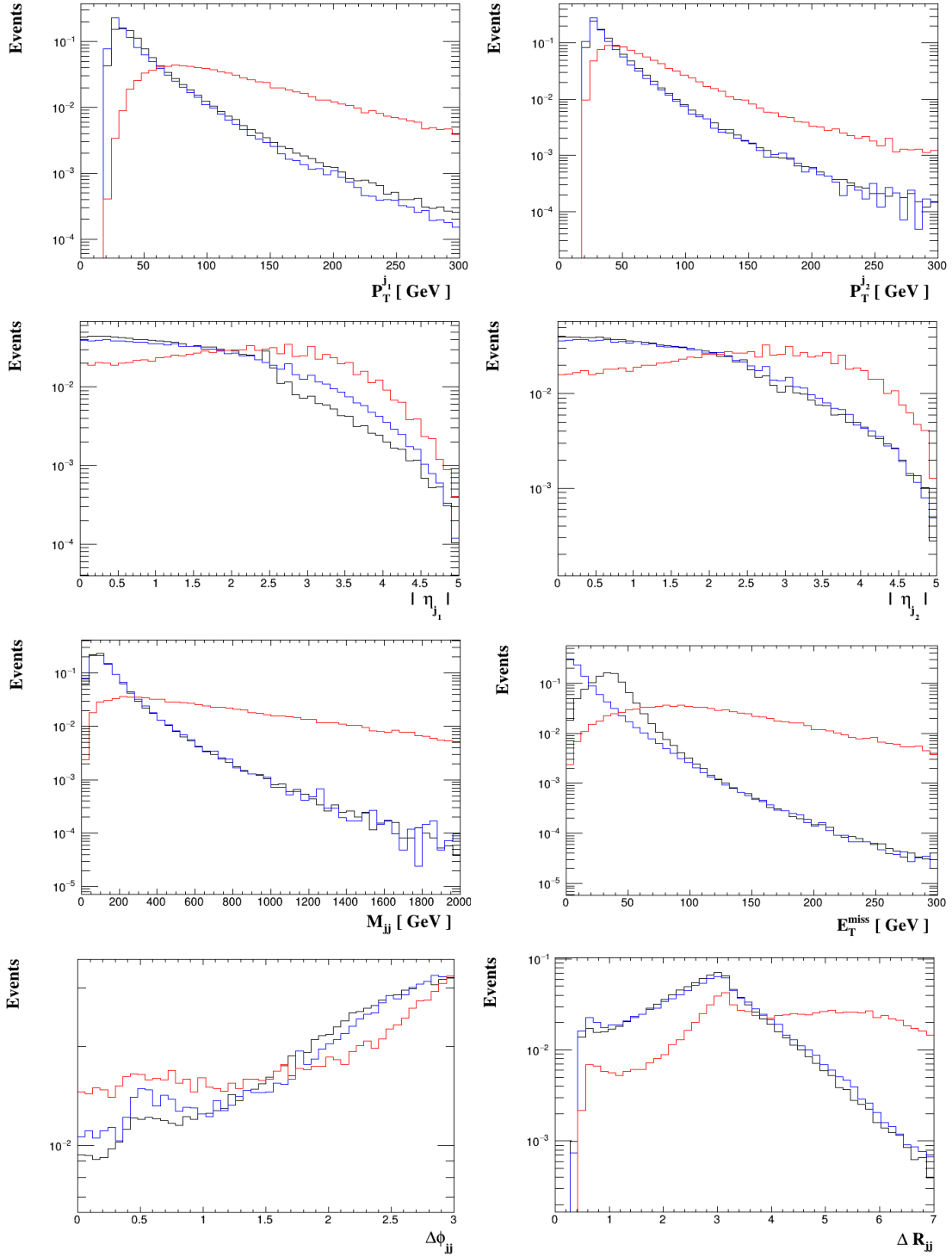


Figure 7: Distribution of the VBF signal and background events, where the signal, W+jets and Z+jets is shown in red, black and blue respectively.

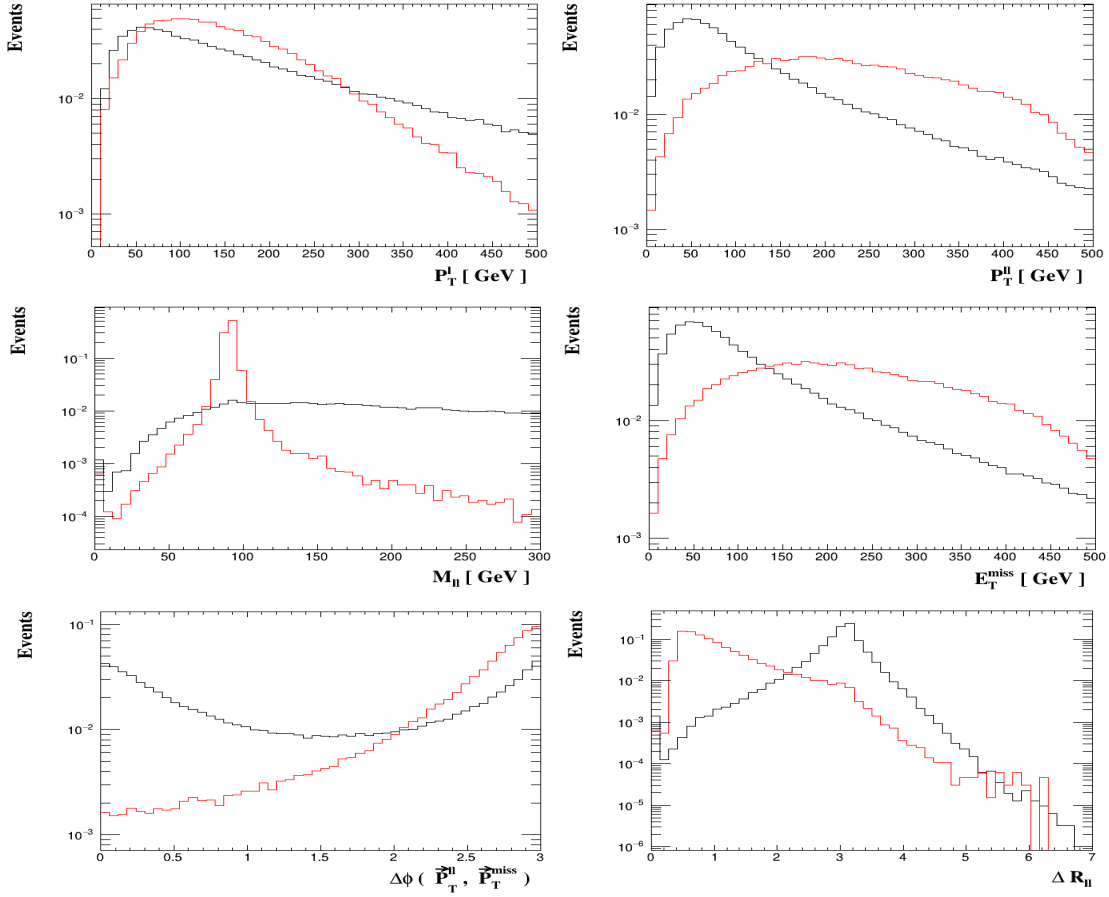


Figure 8: Distribution of the Mono-Z signal and background events, which is shown in red and black respectively.

- [11] D. Cadamuro and J. Redondo, JCAP **02**, 032 (2012), [arXiv:1110.2895 [hep-ph]].
- [12] G. Vertongen and C. Weniger, JCAP **05**, 027 (2011), [arXiv:1101.2610 [hep-ph]].
- [13] R. Essig, E. Kuffik, S. D. McDermott, T. Volansky and K. M. Zurek, JHEP **11**, 193 (2013), [arXiv:1309.4091 [hep-ph]].

- [14] T. Cohen, K. Murase, N. L. Rodd, B. R. Safdi and Y. Soreq, Phys. Rev. Lett. **119**, no.2, 021102 (2017), [arXiv:1612.05638 [hep-ph]].
- [15] X. Yin, S. Xu and S. Zheng, [arXiv:2311.10360 [hep-ph]].
- [16] E. D. Kovetz, V. Poulin, V. Gluscevic, K. K. Boddy, R. Barkana and M. Kamionkowski, Phys. Rev. D **98**, no.10, 103529 (2018), [arXiv:1807.11482 [astro-ph.CO]].
- [17] H. Liu, N. J. Outmezguine, D. Redigolo and T. Volansky, Phys. Rev. D **100**, no.12, 123011 (2019), [arXiv:1908.06986 [hep-ph]].
- [18] T. Hambye, M. H. G. Tytgat, J. Vandecasteele and L. Vanderheyden, Phys. Rev. D **98**, no.7, 075017 (2018), [arXiv:1807.05022 [hep-ph]].
- [19] A. G. Hessler, A. Ibarra, E. Molinaro and S. Vogl, JHEP **01**, 100 (2017), [arXiv:1611.09540 [hep-ph]].
- [20] A. Ghosh, T. Mondal and B. Mukhopadhyaya, JHEP **12**, 136 (2017), [arXiv:1706.06815 [hep-ph]].
- [21] L. Calibbi, L. Lopez-Honorez, S. Lowette and A. Mariotti, JHEP **09**, 037 (2018), [arXiv:1805.04423 [hep-ph]].
- [22] G. Bélanger, N. Desai, A. Goudelis, J. Harz, A. Lessa, J. M. No, A. Pukhov, S. Sekmen, D. Sengupta and B. Zaldivar, *et al.* JHEP **02**, 186 (2019), [arXiv:1811.05478 [hep-ph]].
- [23] G. 't Hooft, NATO Sci. Ser. B **59**, 135-157 (1980).
- [24] V. Silveira and A. Zee, Phys. Lett. B **161**, 136-140 (1985).
- [25] J. McDonald, Phys. Rev. D **50**, 3637-3649 (1994), [arXiv:hep-ph/0702143 [hep-ph]].
- [26] C. P. Burgess, M. Pospelov and T. ter Veldhuis, Nucl. Phys. B **619**, 709-728 (2001), [arXiv:hep-ph/0011335 [hep-ph]].
- [27] J. M. Cline, K. Kainulainen, P. Scott and C. Weniger, Phys. Rev. D **88**, 055025 (2013) [erratum: Phys. Rev. D **92**, no.3, 039906 (2015)], [arXiv:1306.4710 [hep-ph]].
- [28] H. Han and S. Zheng, JHEP **12**, 044 (2015), [arXiv:1509.01765 [hep-ph]].
- [29] H. Han, J. M. Yang, Y. Zhang and S. Zheng, Phys. Lett. B **756**, 109-112 (2016), [arXiv:1601.06232 [hep-ph]].
- [30] N. Aghanim *et al.* [Planck], Astron. Astrophys. **641**, A6 (2020) [erratum: Astron. Astrophys. **652**, C4 (2021)], [arXiv:1807.06209 [astro-ph.CO]].
- [31] G. Alguero, G. Belanger, F. Boudjema, S. Chakraborti, A. Goudelis, S. Kraml, A. Mjallal and A. Pukhov, Comput. Phys. Commun. **299**, 109133 (2024), [arXiv:2312.14894 [hep-ph]].

- [32] J. L. Feng, A. Rajaraman and F. Takayama, Phys. Rev. D **68**, 063504 (2003), [arXiv:hep-ph/0306024 [hep-ph]].
- [33] D. Hooper, F. S. Queiroz and N. Y. Gnedin, Phys. Rev. D **85**, 063513 (2012), [arXiv:1111.6599 [astro-ph.CO]].
- [34] E. Aprile *et al.* [XENON], Phys. Rev. Lett. **121**, no.11, 111302 (2018), [arXiv:1805.12562 [astro-ph.CO]].
- [35] Y. Meng *et al.* [PandaX-4T], Phys. Rev. Lett. **127**, no.26, 261802 (2021), [arXiv:2107.13438 [hep-ex]].
- [36] J. Aalbers *et al.* [LZ], Phys. Rev. Lett. **131**, no.4, 041002 (2023), [arXiv:2207.03764 [hep-ex]].
- [37] M. Aaboud *et al.* [ATLAS], Phys. Rev. Lett. **122**, no.23, 231801 (2019), [arXiv:1904.05105 [hep-ex]].
- [38] S. Chatrchyan *et al.* [CMS], Eur. Phys. J. C **74**, 2980 (2014), [arXiv:1404.1344 [hep-ex]].
- [39] A. Tumasyan *et al.* [CMS], Phys. Rev. D **105**, no.9, 092007 (2022), [arXiv:2201.11585 [hep-ex]].
- [40] G. Aad *et al.* [ATLAS], JHEP **08**, 104 (2022), [arXiv:2202.07953 [hep-ex]].
- [41] E. Conte, B. Fuks and G. Serret, Comput. Phys. Commun. **184**, 222-256 (2013), [arXiv:1206.1599 [hep-ph]].
- [42] V. Khachatryan *et al.* [CMS], Phys. Rev. D **93**, no.5, 052011 (2016) [erratum: Phys. Rev. D **97**, no.9, 099903 (2018)], [arXiv:1511.09375 [hep-ex]].
- [43] A. M. Sirunyan *et al.* [CMS], JHEP **03**, 061 (2017) [erratum: JHEP **09**, 106 (2017)], [arXiv:1701.02042 [hep-ex]].
- [44] A. M. Sirunyan *et al.* [CMS], Eur. Phys. J. C **78**, no.4, 291 (2018), [arXiv:1711.00431 [hep-ex]].
- [45] A. M. Sirunyan *et al.* [CMS], Eur. Phys. J. C **81**, no.1, 13 (2021) [erratum: Eur. Phys. J. C **81**, no.4, 333 (2021)], [arXiv:2008.04735 [hep-ex]].